nature chemistry

ARTICLES

https://doi.org/10.1038/s41557-018-0028-5

Cold quantum-controlled rotationally inelastic scattering of HD with H_2 and D_2 reveals collisional partner reorientation

William E. Perreault, Nandini Mukherjee* and Richard N. Zare*

Molecular interactions are best probed by scattering experiments. Interpretation of these studies has been limited by lack of control over the quantum states of the incoming collision partners. We report here the rotationally inelastic collisions of quantum-state prepared deuterium hydride (HD) with H_2 and D_2 using a method that provides an improved control over the input states. HD was coexpanded with its partner in a single supersonic beam, which reduced the collision temperature to 0–5 K, and thereby restricted the involved incoming partial waves to *s* and *p*. By preparing HD with its bond axis preferentially aligned parallel and perpendicular to the relative velocity of the colliding partners, we observed that the rotational relaxation of HD depends strongly on the initial bond-axis orientation. We developed a partial-wave analysis that conclusively demonstrates that the scattering mechanism involves the exchange of internal angular momentum between the colliding partners. The striking differences between H_2/HD and D_2/HD scattering suggest the presence of anisotropically sensitive resonances.

One of the best ways to study the nature of molecular interactions is to conduct scattering experiments that map the quantum state of the incoming particles to the measured state of the outgoing particles. State-resolved scattering experiments that study single-collision events provide experimental access to molecular interaction potentials because the probability of scattering within a differential solid angle is directly proportional to the square of the scattering matrix element between the input and output states[1,2]. Therefore, the experimental challenge lies in preparing a large molecular population in a desired input state and then state-selectively measuring the angular distribution of the outgoing scattered particles[3–5]. The internal states and orbital angular-momentum states of the outgoing particles can be determined from state-resolved measurements of the angular distribution using well-developed techniques[6–8]. However, full control over the input channel, which is defined by both the internal molecular quantum state and the orbital angular-momentum states associated with the relative motion of the colliding pair, is much more difficult to achieve[9,10].

The internal quantum state of a molecule in a given electronic state is defined in terms of its vibrational and rotational energy, related to quantum numbers (v, j), as well as the projection of the rotational angular momentum j onto a fixed axis, given by the m quantum number. The preparation of states with specific (j, m) defines the molecular frame with respect to a known axis in the lab frame and provides the stereodynamic control necessary to determine the anisotropy of scattering force fields[11]. Many techniques have been developed to control internal quantum states[12], and range from the use of electric[13–16] or magnetic[17] fields[18] for state-selecting molecular populations to techniques that use optical pumping to state-prepare molecules[19–21]. In this work, we use Stark-induced adiabatic Raman passage (SARP) to prepare orientation-specific quantum states of deuterium hydride (HD), a molecule of particular interest because of its abundance in the early universe[22] and theoretical tractability. SARP is an optical adiabatic passage technique developed specifically to state-prepare large populations of small molecules with little or no dipole moment[23,24].

With the prepared molecules in a single quantum state in a sufficiently high density to conduct a scattering experiment, the selection of the orbital angular-momentum states of the incoming particle presents the experimentalist with an additional challenge[10]. Unless the collision energy is reduced substantially, a large number of orbital angular-momentum states in the input channel contribute to the scattering process[25,26]. To preserve the plane-wave character of an incoming particle with well-defined linear momentum, all of the orbital angular momentum l states, also referred to as the partial waves, must be coherently coupled[1,2]. As such, at high collision energies it is necessary to consider the interference of many partial waves in the input channel, which can obscure interesting features of the interaction potential. To gain the clearest possible understanding of the molecular force field, it is therefore necessary to restrict the number of involved input orbital angular-momentum states by reducing the collision temperature. Ultracold collision experiments have succeeded in limiting the input partial waves to only the $l=0$ component[27,28], but, in the absence of the measurement of the output scattering states, it was not possible to truly probe the interaction force field. Molecular-beam technology provides an opportunity to study relatively cold collisions in a wide variety of species and is easily coupled to existing techniques to determine the outgoing scattering states[29]. Many different molecular-beam techniques have been developed to study collisions at relatively low energy, thus reducing the number of involved partial waves. These methods include buffer gas cooling[9], CRESU (reaction kinetics in uniform supersonic flow (cinétique de réaction en ecoulement supersonique uniforme))[30], merged[31] and crossed[10,21,32] beams, and Stark, Zeeman and Faraday deceleration[18]. In this work, we employ a technologically simpler method in which the colliding species are coexpanded in a single molecular beam[33,34]. This brings the collision energy near 1 K, which limits the partial waves to s ($l=0$) and p ($l=1$). In addition, coexpansion of the colliding partners in a single collimated beam defines the direction of their relative velocity within a few milliradians, which is essential for stereodynamic studies.

Department of Chemistry, Stanford University, Stanford, CA, USA. *e-mail: nmukherj@stanford.edu; zare@stanford.edu

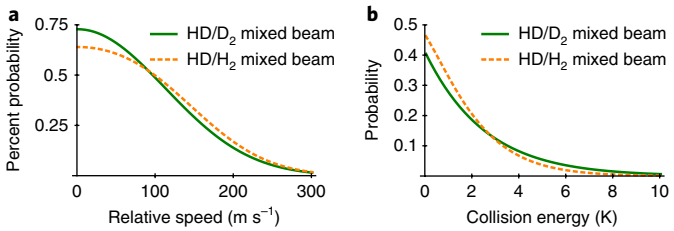

Fig. 1 | Relative-speed and energy distributions. a, Relative-speed distributions between HD ($v=1, j=2$) and D_2 ($v=0, j=0$) (green curve) and HD ($v=1, j=2$) and H_2 ($v=0, j=0$) (orange dashed curve), derived by convolution of the velocity distribution of the two species present in each mixed molecular beam, as determined from time-of-flight measurements. About 85% of the collisions take place with a relative velocity of 160 m s^{-1} or less for both the H_2/HD and D_2/HD mixed beams. When (**a**) is integrated over the relative speeds, the value is 100. **b**, Collision-energy distributions for D_2/HD (green curve) and H_2/HD (orange dashed curve), calculated using the relative-speed distributions in **a**. The two beams have nearly the same range of collision energies present. Greater than 85% of the collisions have a collision energy of less than 5 K.

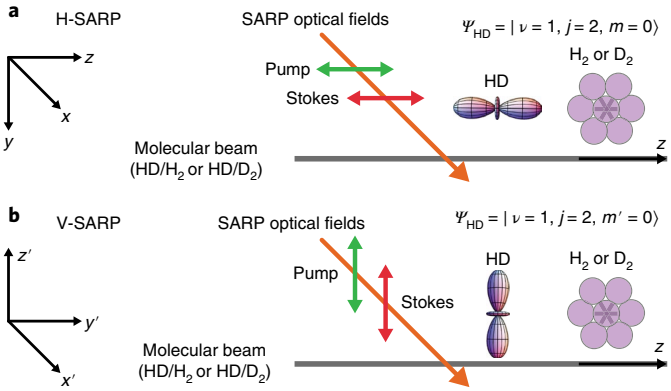

Fig. 2 | Two different collision geometries. a,**b**, The quantum state of HD is prepared using SARP optical fields polarized parallel (H-SARP) (**a**) or perpendicular (V-SARP) (**b**) to the molecular-beam axis. The green and red arrows define the polarization direction of the pump and Stokes optical fields. For H-SARP, the m state refers to the quantization z axis parallel to the relative velocity of HD and its scattering partner. For V-SARP, the m' state refers to the quantization z' axis perpendicular to the relative velocity. For H-SARP, the HD bond axis is preferentially aligned parallel to the relative velocity, and for V-SARP, the HD bond axis is preferentially aligned perpendicular to the relative velocity. The scattering partner (either H_2 or D_2) is not state prepared, so its bond axis is distributed isotropically.

By combining SARP with the coexpansion of the colliding partners in the molecular beam, we are able to control both the internal quantum state (v, j, m) and partial waves of the incoming molecules. We then measure the angular distribution of the scattered molecules state selectively, from which we determine the outgoing states using partial-wave analysis based on the conservation of angular momentum. Our control of the input state coupled with our partial-wave analysis allows us to infer the internal dynamics of a collision process.

In our previous work[33], we demonstrated low-energy molecular scattering in a single beam using quantum-state prepared molecules, and observed remarkable stereodynamic effects in the scattering of HD ($v=1, j=2$) with D_2 to produce HD ($v=1, j=1$). In this paper, we present HD ($v=1, j=2$) collisions with D_2 as well as H_2 to produce HD ($v=1, j=0$), and find that a simultaneous reorientation of the partner molecule is necessary to explain our experimental data. Our previous paper focused primarily on the experimental method, and the present publication illustrates how details of the anisotropic scattering potential can be extracted directly from quantum-state resolved, low-energy scattering measurements by correlating each input partial wave with the measured outgoing waves using partial-wave analysis. We determined the dominant anisotropies responsible for $\Delta j=2$ inelastic scattering, which include a strong short-range and a relatively weaker long-range potential term that results from quadrupole–quadrupole interactions. This distinguishes the $\Delta j=2$ transition studied here from the previously studied $\Delta j=1$ transition, which results primarily from dipolar interactions.

Results

Experimental results. Figure 1a shows the relative-speed distributions between HD and its scattering partner in the two mixed-molecular beams (1:6 HD:D_2 and 1:8 HD:H_2), which are calculated from time-of-flight measurements of HD, D_2 and H_2 following (2+1) resonance-enhanced multiphoton ionization (REMPI). To determine the velocity distribution of the neutral molecules accurately, the REMPI photoelectron recoil was deconvoluted from the measured time-of-flight spectra[35]. Figure 1b shows the corresponding collision-energy distribution for D_2/HD and H_2/HD, calculated using the relative-speed distributions in Fig. 1a. The rotational distributions of each species in the molecular beam are given in Supplementary Table 1.

We used SARP to prepare specific m states of the rovibrationally excited ($v=1, j=2$) energy eigenstate of the HD molecules. SARP employs a delayed sequence of single-mode nanosecond pump and Stokes laser pulses that transversely intersect the molecular beam to transfer adiabatically the complete ground-state population to specific-energy eigenstates[23,36]. The molecular alignment was controlled by changing the direction of the polarization of the pump and Stokes optical fields[24]. As the HD is so efficiently cooled to its rotational ground state, we were able to transfer nearly the entire population to the rovibrationally excited ($v=1, j=2, m$) state using SARP. The colliding partner (either H_2 or D_2) was not state selected.

For each scattering partner, we studied the rotational relaxation of state-prepared HD from ($v=1, j=2$) → ($v=1, j=0$) for the HD bond axis preferentially aligned parallel or perpendicular to the relative velocity direction. Figure 2 shows the parallel and perpendicular collision geometries, denoted by H-SARP and V-SARP. In H-SARP (Fig. 2a), the HD ($v=1, j=2$) molecular-bond axis is aligned preferentially parallel to the flight direction using linearly polarized pump and Stokes laser pulses with their direction of polarization aligned along the molecular-beam axis. In V-SARP (Fig. 2b), the HD ($v=1, j=2$) molecular-bond axis is aligned preferentially perpendicular to the flight direction using pump and Stokes laser pulses polarized perpendicularly with respect to the molecular-beam axis. The colliding partners are coexpanded in a single molecular beam, so the direction of their relative velocity is extremely well defined (±12 mrad).

Figure 3 shows the angular distribution produced by the rotational relaxation of HD molecules from ($v=1, j=2$) → ($v=1, j=0$) in collisions with D_2 in the mixed molecular beam. Figure 3a shows the collisional relaxation of HD prepared by H-SARP, whereas Fig. 3b shows the relaxation for HD prepared by V-SARP, as defined in Fig. 2. The angular distributions shown here were extracted from experimentally measured time-of-flight distributions of scattered HD molecules after state-selective ionization of the scattered HD ($v=1, j=0$) using (2+1) REMPI. The details of the procedure to extract the scattering angle from the time-of-flight measurement are given elsewhere[33]. We observe that there is a notable stereodynamic difference in the differential scattering cross sections between H-SARP and V-SARP, and also that the integral cross section for H-SARP is almost four times smaller than that for V-SARP.

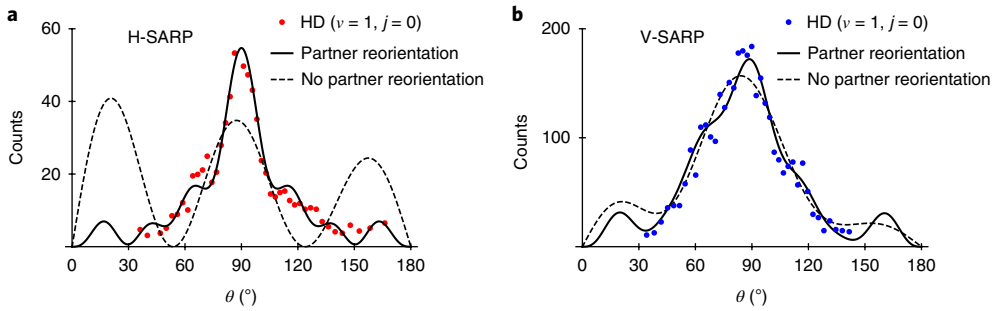

Fig. 3 | D_2/HD mixed-beam scattering. a,**b**, Collisions of the state-prepared HD ($v=1, j=2$) with unprepared D_2 occurred with a mean collision energy of ~1K, with the HD molecular-bond axis aligned parallel (H-SARP) (**a**) and perpendicular (V-SARP) (**b**) to the relative velocity between HD and D_2. The red (**a**) and blue (**b**) points show the angular distribution of the scattered HD ($v=1, j=0$) derived from time-of-flight measurements of REMPI-generated ions. In both **a** and **b**, the dashed curves give theoretical fits generated using functions that neglect D_2 reorientation, and the solid curves give theoretical fits generated using functions that include D_2 reorientation, as described in the main text. In addition to the obvious stochasticity in the number of counts in each bin, the scattering angle is subject to a small (<5%) error from the finite width of the molecular beam, but this does not affect the fits shown here.

Partial-wave analysis. To interpret the angular distributions, we employed a similar partial-wave analysis to that described in our earlier work on HD ($v=1, j=2$) → HD ($v=1, j=1$) rotationally inelastic scattering[33]. As before, we considered only the s ($l=0$) and p ($l=1$) partial waves in the input channel. Using the H_2/HD and D_2/HD relative-speed distributions (Fig. 1a), we find that for ~85% of collisions the ($l=1$) partial wave corresponds to an impact parameter greater than 3.5 Å for D_2/HD and 4.7 Å for H_2/HD, whereas the ($l=2$) partial wave corresponds to an impact parameter greater than 6 Å and 8.1 Å, respectively. Previously calculated rigid-rotor potentials for H_2–H_2 collisions show that all the anisotropic terms are negligible at distances greater than 5 Å (ref. [37]), which justifies neglecting the input partial waves with ($l>1$) for the collision temperatures present in our experiments.

The collision partners copropagate in a single molecular beam, so the relative velocity direction coincides with the lab-fixed molecular-beam axis, which is parallel to the laser polarization used in the H-SARP preparation. Choosing the angular momentum to be quantized along the relative velocity axis considerably simplifies the data analysis because the initial orbital angular-momentum component vanishes in this direction. In this frame, the HD ($v=1, j=2$) state prepared by H-SARP is simply $|j=2, m=0\rangle$ where m refers to the angular-momentum component along the z axis in Fig. 2a. The state prepared by V-SARP, when transformed into this coordinate system, is given by:

$$|j=2, m'=0\rangle = \sqrt{\frac{3}{8}}\,|j=2, m=+2\rangle - \frac{1}{2}|j=2, m=0\rangle + \sqrt{\frac{3}{8}}\,|j=2, m=-2\rangle \quad (1)$$

where m' refers to the angular-momentum component along the z' axis, which is parallel to the laser polarization direction in the V-SARP preparation, as described in Fig. 2b. The vibrational quantum number ($v=1$) is omitted for simplicity.

The ($j=2 \rightarrow j=0$) scattering angular distribution $d\sigma/d\theta$ as a function of the polar angle θ, which was determined from time-of-flight spectrometry, is related to the differential scattering cross section $d\sigma/d\Omega$ by integration over all azimuthal angles φ:

$$\frac{d\sigma}{d\theta} = \sin\theta \int_0^{2\pi} \left(\frac{d\sigma}{d\Omega}\right) d\varphi \quad (2)$$

where $d\Omega$ gives the differential solid angle in the direction defined by θ and φ. The differential cross sections can be expressed in terms of the state-to-state scattering amplitudes ($q_{j=2,m\rightarrow j=0}$), as follows. For H-SARP:

$$\left(\frac{d\sigma}{d\Omega}\right)^{H} = |q_{j=2,m=0\rightarrow j=0}|^2 \quad (3)$$

and for V-SARP:

$$\left(\frac{d\sigma}{d\Omega}\right)_{V} = \left| \sqrt{\frac{3}{8}}\, q_{j=2,m=+2\rightarrow j=0} - \frac{1}{2} q_{j=2,m=0\rightarrow j=0} + \sqrt{\frac{3}{8}}\, q_{j=2,m=-2\rightarrow j=0} \right|^2 \quad (4)$$

Each state-to-state scattering amplitude can be expanded in terms of the outgoing partial waves ($l', m_{l'}$) which are given by the spherical harmonics $Y_{l',m_{l'}}(\theta,\varphi)$as described in the Supplementary Information. Here, l' and $m_{l'}$ are the quantum numbers associated with the outgoing orbital angular momentum and its component along the quantization z axis, respectively. Equations (3) and (4) can then be substituted into equation (2) to produce the fitting functions used to generate the theoretical curves in Fig. 3, as well as those in Fig. 4. The dashed curves in Fig. 3 show fits of the experimental data in which the expansion of the scattering amplitudes in terms of partial waves assumed that no exchange of angular momentum occurred between HD and D_2. This procedure clearly failed to fit the H-SARP data accurately ($R^2=0.73$). Although the fit of the V-SARP data generated using this procedure appears to be reasonable ($R^2=0.98$), it clearly fails to reproduce the sharpness of the peak at 90°, and also misses the two shoulders that appear near 60° and 120°. Consideration of the conservation of the angular-momentum component along the z axis shows that the strong scattering peak near 90° necessitates the involvement of outgoing partial waves with ($m_{l'} \neq 0$). For molecules prepared by V-SARP, these outgoing partial waves are generated by the direct relaxation of the initial HD ($v=1$, $j=2$, $m=\pm 2$) state, which explains the relatively good fit shown by the dashed curve in Fig. 3b. In the H-SARP case, however, these outgoing partial waves can only be produced via the exchange of angular momentum between the two scattering partners.

Partner reorientation explains experimental observations. To obtain a better fit of our H-SARP data, we introduced into our

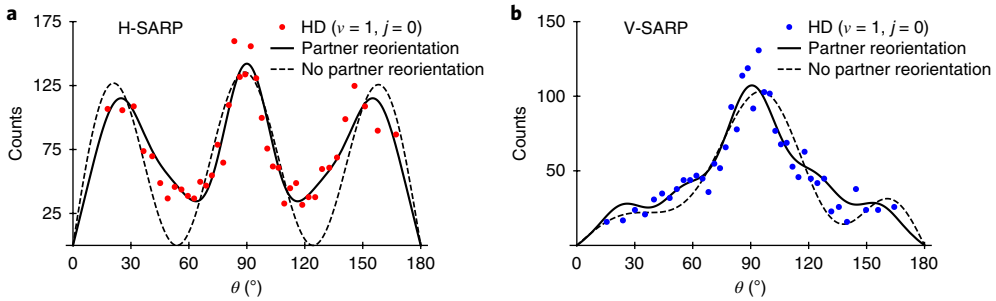

Fig. 4 | H_2/HD mixed-beam scattering. a,**b**, Collisions of state-prepared HD ($v=1$, $j=2$) with unprepared H_2 occurred with a mean collision energy of ~1K, with the HD molecular-bond axis aligned parallel (H-SARP) (**a**) and perpendicular (V-SARP) (**b**) to the relative velocity between HD and H_2. The red (**a**) and blue (**b**) points show the angular distribution of the scattered HD ($v=1$, $j=0$) derived from time-of-flight measurements of REMP-generated ions. In both **a** and **b**, the dashed curves give the theoretical fits generated using functions that neglect H_2 reorientation, and the solid curves give theoretical fits generated using functions that include H_2 reorientation, as described in the main text. In addition to the obvious stochasticity in the number of counts in each bin, the scattering angle is subject to a small (<5%) error from the finite width of the molecular beam, but this does not affect the fits shown here.

partial-wave analysis the simultaneous degenerate ($\Delta j=0$) reorientation transitions $\Delta m=\pm1$ and ±2 in D_2 ($v=0$, $j=1$) and D_2 ($v=0$, $j=2$), respectively, that accompany the rotational relaxation of HD ($v=1$, $j=2$) → HD ($v=1$, $j=0$). When these degenerate reorientations were considered for H-SARP, we obtained the solid curve in Fig. 3a, which shows a substantially better fit to the experimental data ($R^2=0.98$). A similar reorientational angular-momentum exchange was then considered for the relaxation of the HD ($v=1$, $j=2$, $m=0$) component present in the superposition prepared by V-SARP (equation (1)), which resulted in the slightly improved fit given by the solid curve in Fig. 3b ($R^2=0.99$). Table 1 summarizes the outgoing partial waves that contribute to each of the reorientation fits.

Although these degenerate reorientations explain the experimental data well, there is another open output channel that involves angular-momentum exchange, which could support the 90° scattering peak we see for H-SARP. This output channel involves the simultaneous nonresonant rotational excitation of D_2 from ($v=0$, $j=0$) → ($v=0$, $j=2$) that accompany HD relaxation from ($v=1$, $j=2$) → ($v=1$, $j=0$). However, the following consideration of the energetics of the collision shows that this mechanism is unlikely to contribute to the observed scattering. The maximum speed of the scattered HD molecules along the time-of-flight axis can be determined from the energy released in the collision. Clearly, the mechanism that involves the excitation of D_2 will result in a smaller final HD speed than the D_2 reorientation mechanism because a significant portion of the energy produced by rotational relaxation of HD ($v=1$, $j=2$) → HD ($v=1$, $j=0$) is absorbed by the D_2 excitation. However, the experimental time-of-flight spectrum shows the presence of scattered HD molecules with speeds along the time-of-flight axis that exceed the maximum allowed by the mechanism involving D_2 excitation. On the other hand, the observed speeds fall well within the range allowed by the D_2 reorientation mechanism. This suggests that the likely mechanism is the reorientation rather than the excitation of D_2. To determine conclusively that the mechanism is reorientation of D_2, we examined the H_2/HD scattering because the energy released by the rotational relaxation of HD ($v=1$, $j=2$) → HD ($v=1$, $j=0$) is insufficient to rotationally excite H_2. Our analysis of the H_2/HD scattering data, which also necessitated angular-momentum exchange, as detailed below, provides additional evidence that the mechanism is the reorientation rather than the excitation of D_2.

Figure 4 gives the angular distribution of the rotational relaxation of HD ($v=1$, $j=2$) → HD ($v=1$, $j=0$) produced by collisions with coexpanded H_2. Figure 4a,b show the angular distribution of the collisional relaxation for the initial state of HD prepared by H-SARP and V-SARP, respectively. Not only is there a notable stereodynamic difference in the differential cross sections between H-SARP and V-SARP, comparison with Fig. 3 shows significant differences between H_2/HD and D_2/HD scattering, especially for H-SARP. In further contrast to the D_2/HD scattering, the measured integral cross section for H-SARP is nearly twice that of V-SARP. This is somewhat surprising because the scattering potentials generated by H_2 and D_2 are expected to be very similar unless there is a strong resonance effect.

As in Fig. 3, the dashed curves in Fig. 4 shows fits that were obtained using partial-wave analysis assuming that no angular momentum is exchanged between HD and H_2. Although this procedure provided a somewhat reasonable fit ($R^2=0.96$) of the V-SARP experimental angular distribution, it clearly failed to fit the H-SARP data accurately ($R^2=0.90$). When H_2 degenerate reorientations were included for H-SARP, we obtained the solid curve in Fig. 4a which shows a substantially better fit to the experimental data ($R^2=0.98$). A similar reorientational angular-momentum exchange was then considered for the relaxation of the HD ($v=1$, $j=2$, $m=0$) component of the superposition (equation (1)) prepared by V-SARP, which resulted in the slightly improved fit given by the solid curve in Fig. 4b ($R^2=0.98$). Table 1 summarizes the outgoing partial waves that contribute to each of the reorientation fits for the H_2/HD collisions.

The necessity of H_2 reorientations to fit both the H-SARP and V-SARP data for H_2/HD scattering clearly confirms that partner reorientation is a viable mechanism for these collisions. Additionally, because the H_2/HD H-SARP scattering is relatively strong, we conclude that the cross section for reorientation scattering is significant. This proves that D_2/HD relaxation is mediated by partner reorientation rather than by D_2 excitation.

Table 1 shows that for the D_2/HD collision with HD prepared by H-SARP, the rotational relaxation proceeds entirely via partner reorientation, whereas the relaxation of HD prepared by V-SARP proceeds via two distinct mechanisms, namely, direct relaxation in addition to partner reorientation. As noted above, the direct relaxation is produced by the initial V-SARP-prepared HD ($v=1$, $j=2$, $m=\pm2$) component (equation (1)), whereas the partner-reorientation mechanism comes from the relaxation of the HD ($v=1$, $j=2$, $m=0$) component. In contrast, for H_2/HD collisions, both H-SARP and V-SARP scattering involve the direct as well as the reorientation mechanism. In each of the HD ($j=2$) to HD ($j=0$) scattering cases presented in Table 1, the bold type gives the dominant outgoing partial wave, which was determined from the relative significances given in Supplementary Tables 2–5. Given the angular-momentum conservation in the relaxation of the state HD ($v=1$, $j=2$, $m=0$, ±2) → HD ($v=1$, $j=0$, $m=0$), it is not surprising that the dominant outgoing partial waves are Y_{22} and Y_{20}. For three of the four

Table 1 | Outgoing partial waves

	D_2/HD H-SARP (Fig. 3a)	D_2/HD V-SARP (Fig. 3b)	H_2/HD H-SARP (Fig. 4a)	H_2/HD V-SARP (Fig. 4b)
No partner reorientation $\Delta m=0$	—	**Y_{22}**, Y_{32}	**Y_{20}**	**Y_{22}**, Y_{32}, Y_{20}
Partner reorientation $\Delta m=\pm1$	Y_{11}, Y_{31}, Y_{51}, Y_{71}	Y_{31}, Y_{71}	Y_{11}, Y_{51}	Y_{51}
Partner reorientation $\Delta m=\pm2$	**Y_{22}**	Y_{22}	Y_{22}, Y_{42}	Y_{22}, Y_{42}

Each column gives the outgoing partial waves that contribute to the fits shown in the solid curves in Figs. 3 and 4. Within each column, the partial waves are separated according to the internal mechanism that produced them. Bold type indicates the dominant outgoing partial wave.

cases considered here, the dominant outgoing partial wave is Y_{22}. Only in the case of H_2/HD H-SARP scattering is the dominant partial wave Y_{20}, which suggests a fundamentally different character to this interaction.

Discussion

By connecting each incoming state with each outgoing state using a H_2–H_2 rigid rotor potential (Supplementary Tables 6–9), we were able to associate each outgoing partial wave with the potential terms capable of producing it. We found that all the outgoing partial waves with no partner reorientation (direct relaxation) result from the strongest anisotropic potential term previously calculated by Buck and co-workers[37,38]. Consistent with this, for V-SARP-prepared HD scattering with both collision partners, the dominant partial waves in the scattering angular distribution are Y_{22} arising from the non-reorienting relaxation of HD ($v=1$, $j=2$, $m=\pm2$) present in the input channel (equation (1)). It is likely because of the dominance of the direct relaxation that the differential cross sections for V-SARP in H_2/HD and D_2/HD are similar. In contrast, all outgoing partial waves associated with reorienting collisions correlate with weaker terms in the potential calculated by Buck and co-workers[37,38], the strongest of which arises from long-range quadrupole–quadrupole interactions. The relative strength of the potential term responsible for the nonreorienting collisions readily explains why some of the partial waves associated with partner reorientation in H-SARP scattering do not appear in the analysis of the V-SARP scattering angular distributions. Even though HD has a small permanent dipole moment, our partial-wave analysis shows no terms that correlate with dipole–quadrupole interactions are expected for the HD ($v=1$, $j=2$) → HD ($v=1$, $j=0$) rotational relaxation (Supplementary Section 3.2).

We have also performed measurements on the $\Delta j=1$ transitions in the HD/H_2 beam. Interestingly, they show, within experimental error, the same angular distributions as those measured for the $\Delta j=1$ transitions in the HD/D_2 beam in our earlier work[33]. In contrast, we observe dramatic differences in the $\Delta j=2$ transition between HD/H_2 and HD/D_2 scattering when the HD molecular axis is aligned parallel to the relative velocity. This emphasizes that entirely different anisotropies drive the two inelastic transitions. Additionally, given that H_2 and D_2 have nearly equal quadrupole moments, this highlights an important difference in the dynamics of the $\Delta j=2$ transition between HD/H_2 scattering and HD/D_2 scattering.

Quantum-state-resolved scattering coupled with partial-wave analysis not only elucidates the mechanism of rotationally inelastic diatom–diatom scattering, but also allows us to extract the important anisotropic potential terms directly from experimental measurements. We find that, depending on the initial alignment of the HD molecules, the collisions with H_2 and D_2 molecules involve different parts of the anisotropic potential, and, as a result, produce different outgoing partial waves. As noted above, the dominant partial wave for HD/H_2 H-SARP scattering is Y_{20}, which arises from a direct relaxation that correlates with the strongest anisotropy, as opposed to the dominant wave for D_2/HD H-SARP scattering, Y_{22}, which correlates with weaker anisotropic potential terms. This correlates with the large observed differences between H-SARP-prepared HD scattering with D_2 and H_2 in both the scattering angular distribution and the integral cross section relative to V-SARP.

As the collision energies are so similar (see Fig. 1b), the observed differences between H_2/HD and D_2/HD scattering may originate from the difference in reduced mass. The reduced mass controls the height of the centrifugal barrier, which affects the classical turning point and determines the range of the potential probed by the scattering process. The centrifugal barrier, which is particularly important for collision energies in the range of a few Kelvin, can give rise to orbiting resonances. These resonances were predicted theoretically for H_2/HD collisions[39,40], so their presence is not unexpected, but they had not been measured experimentally. A strong dependence of resonance on reduced mass has been observed in the Penning ionization of the hydrogen isotopologues by metastable helium atoms[41]. Although the present work does not directly measure resonances, we believe that, in showing that small changes in reduced mass cause large changes in the scattering distribution it provides experimental evidence suggesting their presence. We have also considered the fact that the difference of *para* and *ortho* distributions for normal H_2 and D_2 may also give rise to the observed difference in the scattering of HD with H_2 compared to D_2. Although a large population of H_2 (~ 75%) can be found in the ($v=0$, $j=1$) state, a relatively small fraction of D_2 is in ($v=0$, $j=1$) (33%), and ($v=0$, $j=2$) (~8%) having substantial quadrupole moments to cause efficient transition. However, this difference of *ortho* and *para* distributions can only affect the intensity of scattering; it cannot fully explain the dramatic difference observed in the shape of the scattering angular distribution of HD with H_2 and D_2 for HSARP. On the other hand, in presence of resonance, there will be a substantial induced quadrupole moment making a more profound difference in the scattering angular distribution. The presence of the possible resonance is further supported by the uniqueness of Y_{20} as the dominant partial wave in H_2/HD H-SARP scattering, which further indicates that any collisional resonance is highly orientationally dependent. However, none of the prior theoretical studies have examined the effects of anisotropy in collisional resonances. These results truly emphasize the importance of fully quantum-state-resolved scattering experiments at low collision energies to elucidate the most fundamental aspects of molecular interaction potentials.

Methods

A mixture of HD (98% (Cambridge Isotope Labs)) and either D_2 (99.6% (Cambridge Isotope Labs)) or H_2 (99.999% (Praxair)) was coexpanded in a high-vacuum source chamber using a room-temperature Even–Lavie pulsed valve at a stagnation pressure of 11 bar. To reduce the transverse velocity spread of the molecular beam, we collimated the beam using a skimmer of diameter 600 μm, kept at a distance of ~8 cm from the pulsed valve. The skimmer opening was located ~35 mm upstream of the interaction region. Using ($v=0$, $j=0$) REMPI, we measured the diameter of the molecular beam in the interaction region to be ~1.5 mm. This allowed us to determine the transverse beam divergence to be ~12 mrad, which corresponds to a transverse velocity spread of ~26 m s^{-1}. As such, the coexpansion not only brought the collision energy down to near 1 K, which significantly reduces the number of involved partial waves, but also allowed us to define the relative velocity of the colliding partners, and so considerably simplify the analysis of the scattering angular distribution.

HD molecules were prepared in the ($v=1$, $j=2$, m) state using SARP. SARP accomplishes a complete population transfer using a sequence of partially

overlapping single-mode pump and Stokes laser pulses. By inducing a second-order Stark shift of the rovibrational levels, the stronger pump pulse (10 ns, 532 nm, 10 J mm^{-2}) sweeps the Raman frequency through resonance twice during the rising and falling of its intensity. The population is transferred adiabatically from HD ($v=0, j=0$) to HD ($v=1, j=2, m=0$) in the presence of the Stokes pulse (5 ns, 670 nm, 2 J mm^{-2}) at the second resonance crossing, as long as the frequency difference between the pump and Stokes laser pulses is tuned to within a few gigahertz of the Raman resonance in HD (116.546 THz). SARP requires a threshold laser power to satisfy the condition of adiabatic following defined by $d\Delta / dt < 2\pi\omega_R^2$ where ω_R is the Rabi frequency for the HD ($v=0, j=0$) to HD ($v=1, j=2$) Raman transition and $d\Delta/dt$ is the Stark-induced sweeping rate of dynamic Raman detuning Δ. More-detailed descriptions of SARP can be found elsewhere[23,24,36]. The pump pulse was obtained from the second harmonic of an injection-seeded, Q-switched Nd^{3+}:YAG laser (PRO-290 (Spectra-Physics)), and the Stokes pulse was derived from a pulsed dye amplifier (PrecisionScan (Sirah)) seeded by a frequency-stabilized ring dye laser (Matisse (Sirah)) and pumped by the same Nd^{3+}:YAG laser used to generate the pump pulse. After an optical delay of 6 ns, the Stokes laser pulse was combined with the pump pulse on a dichroic beam splitter. Both beams were then focused onto the molecular beam using a 40 cm focal length lens. The region of the molecular beam excited by SARP was experimentally measured to have a diameter of ~100 μm.

The scattering products were probed using a third laser pulse to state-selectively ionize HD molecules by (2+1) REMPI. The REMPI probe beam (5 ns, 209 nm, 0.3 J mm^{-2}) was focused onto the molecular beam using a 60 cm lens to a spot size of ~20 μm. The REMPI pulse was obtained by using two different β-barium borate crystals in sequence to generate the third harmonic of a tunable pulsed dye laser (ND6000 (Continuum Lasers, Inc.)) pumped by a Q-switched Nd^{3+}:YAG laser (PL9020, Continuum Lasers, Inc.). The probe polarization was held perpendicular to the time-of-flight axis to minimize the contribution of photoelectron recoil velocity[35] to the measured time-of-flight spectrum. The REMPI-generated ions were detected on a multichannel plate at the end of a time-of-flight mass spectrometer connected to the reaction chamber. The velocity distribution of the scattered molecules along the molecular beam axis was determined directly from the measured time-of-flight spectrum. As the scattering centre-of-mass frame coincides with the moving frame of reference of the molecular beam, the scattering angular distribution can then be easily extracted from the velocity distribution using the final speed of the scattered HD molecules calculated using the conservation of energy[33].

Data availability. The experimental data supporting this study are available from N.M. on request.

Received: 10 October 2017; Accepted: 16 February 2018;
Published online: 16 April 2018

References

1. Blatt, J. M. & Biedenharn, L. C. The angular distribution of scattering and reaction cross sections. *Rev. Mod. Phys.* **24**, 258–272 (1952).
2. Arthurs, A. M. & Dalgarno, A. The theory of scattering by a rigid rotator. *Proc. R. Soc. A* **256**, 540–551 (1960).
3. Warren, W. S., Rabitz, H. & Dahleh, M. Coherent control of quantum dynamics: the dream is alive. *Science* **259**, 1581–1589 (1993).
4. Zare, R. N. Laser control of chemical reactions. *Science* **279**, 1875–1879 (1998).
5. PanH., Wang, F,. Czakó, G. & Liu, K. Direct mapping of the angle-dependent barrier to reaction for Cl + CHD_3 using polarized scattering data. *Nat. Chem.* **9**, 1175–1180 (2017).
6. Smith, G. P. & Zare, R. N. Angular distribution of product internal states using laser fluorescence detection: the Ba + KCl reaction. *J. Chem. Phys.* **64**, 2632–2640 (1976).
7. Lin, J. J., Zhou, J., Shiu, W. & Liu, K. State-specific correlation of coincident product pairs in the F + CD_4 reaction. *Science* **300**, 966–969 (2003).
8. Bartlett, N. C.-M. et al. Differential cross sections for H + D_2 → HD(v' = 2, j' = 0,3,6,9) + D at center-of-mass collision energies of 1.25, 1.61, and 1.97 eV. *Phys. Chem. Chem. Phys.* **13**, 8175–8179 (2011).
9. Stuhl, B. K., Hummon, M. T. & Ye, J. Cold state-selected molecular collisions and reactions. *Annu. Rev. Phys. Chem.* **65**, 501–518 (2014).
10. Naulin, C. & Costes, M. Experimental search for scattering resonances in near cold molecular collisions. *Int. Rev. Phys. Chem.* **33**, 427–446 (2014).
11. Aoiz, F. J. et al. A new perspective: imaging the stereochemistry of molecular collisions. *Phys. Chem. Chem. Phys.* **17**, 30210–30228 (2015).
12. Loesch, H. J. Orientation and alignment in reactive beam collisions: recent progress. *Annu. Rev. Phys. Chem.* **46**, 555–594 (1995).
13. Jones, E. M. & Brooks, P. R. Focusing and orienting asymmetric-top molecules in molecular beams. *J. Chem. Phys.* **53**, 55–58 (1970).
14. Loesch, H. J. & Remscheid, A. Brute force in molecular reaction dynamics: a novel technique for measuring steric effects. *J. Chem. Phys.* **93**, 4779 (1990).
15. van Leuken, J. J., van Amerom, F. H. W., Bulthuis, J., Snijders, J. G. & Stolte, S. Parity-resolved rotationally inelastic collisions of hexapole state-selected NO ($^2\Pi_{1/2}$, J = 0.5) with Ar. *J. Phys. Chem.* **99**, 15573–15579 (1995).
16. Brouard, M. et al. Fully quantum state-resolved inelastic scattering of NO(X) + Kr: differential cross sections and product rotational alignment. *J. Chem. Phys.* **141**, 164306 (2014).
17. Watanabe, D., Ohoyama, H., Matsumura, T. & Kasai, T. Effect of mutual configuration between molecular orientation and atomic orientation in the oriented Ar + oriented CF_3H reaction. *Phys. Rev. Lett.* **99**, 1–4 (2007).
18. Brouard, M., Parker, D. H. & van de Meerakker, S. Y. T. Taming molecular collisions using electric and magnetic fields. *Chem. Soc. Rev.* **43**, 7279–7294 (2014).
19. Rohlfing, E. A., Chandler, D. W. & Parker, D. H. Direct measurement of rotational energy transfer rate constants for HCl (v = 1). *J. Chem. Phys.* **87**, 5229–5237 (1987).
20. Dittmann, P. et al. The effect of vibrational excitation ($3 \leq v' \leq 19$) on the reaction Na_2 (v') + Cl → NaCl + Na*. *J. Chem. Phys.* **97**, 9472 (1992).
21. Liu, K. Perspective: vibrational-induced steric effects in bimolecular reactions. *J. Chem. Phys.* **142**, 80901 (2015).
22. Palla, F., Galli, D. & Silk, J. Deuterium in the universe. *Astrophys. J.* **451**, 44–50 (1995).
23. Dong, W., Mukherjee, N. & Zare, R. N. Optical preparation of H_2 rovibrational levels with almost complete population transfer. *J. Chem. Phys.* **139**, 74204 (2013).
24. Mukherjee, N., Dong, W. & Zare, R. N. Coherent superposition of M-states in a single rovibrational level of H_2 by Stark-induced adiabatic Raman passage. *J. Chem. Phys.* **140**, 74201 (2014).
25. Weck, P. F. & Balakrishnan, N. Importance of long-range interactions in chemical reactions at cold and ultracold temperatures. *Int. Rev. Phys. Chem.* **25**, 283–311 (2006).
26. Quéméner, G, Balakrishnan, N. & Dalgamo, A. in Stwalley, W. C., Krems, R. V. & Friedrich, B. (eds) *Cold Molecules: Theory, Experiment, Applications* 69–124 (CRC, Boca Raton, 2009)..
27. Krems, R. V. Cold controlled chemistry. *Phys. Chem. Chem. Phys.* **10**, 4079–4092 (2008).
28. de Miranda, M. H. G. et al. Controlling the quantum stereodynamics of ultracold bimolecular reactions. *Nat. Phys.* **7**, 502–507 (2011).
29. van de Meerakker, S. Y., Bethlem, H. L., Vanhaecke, N. & Meijer, G. Manipulation and control of molecular beams. *Chem. Rev.* **112**, 4828–4878 (2012).
30. Rowe, B. R. & Marquette, J. B. CRESU studies of ion/molecule reactions. *Int. J. Mass Spectrom. Ion. Process* **80**, 239–254 (1987).
31. Shagam, Y. et al. Molecular hydrogen interacts more strongly when rotationally excited at low temperatures leading to faster reactions. *Nat. Chem.* **7**, 921–926 (2015).
32. Chefdeville, S. et al. Observation of partial wave resonances in low-energy O_2–H_2 inelastic collisions. *Science* **341**, 1094–1096 (2013).
33. Perreault, W. E., Mukherjee, N. & Zare, R. N. Quantum control of molecular collisions at 1 kelvin. *Science* **358**, 356–359 (2017).
34. Amarasinghe, C. & Suits, A. G. Intrabeam scattering for ultracold collisions. *J. Phys. Chem. Lett.* **8**, 5153–5159 (2017).
35. Perreault, W. E., Mukherjee, N. & Zare, R. N. Angular and internal state distributions of H_2^+ generated by (2 + 1) resonance enhanced multiphoton ionization of H_2 using time-of-flight mass spectrometry. *J. Chem. Phys.* **144**, 214201 (2016).
36. Perreault, W. E., Mukherjee, N. & Zare, R. N. Preparation of a selected high vibrational energy level of isolated molecules. *J. Chem. Phys.* **145**, 154203 (2016).
37. Buck, U., Huisken, F., Maneke, G. & Schaefer, J. State resolved rotational excitation in HD + D_2 collisions. I. Angular dependence of 0→2 transitions. *J. Chem. Phys.* **74**, 535–544 (1981).
38. Buck, U. Rotationally inelastic scattering of hydrogen molecules and the non-spherical interaction. *Faraday Discuss. Chem. Soc.* **73**, 187–203 (1982).
39. Schaefer, J. Rotational integral cross sections and rate coeffients of HD scattered by He and H_2. *Astron. Astrophys. Suppl. Ser.* **85**, 1101–1125 (1990).
40. Lee, T.-G. et al. State-to-state rotational transitions in H_2 + H_2 collisions at low temperatures. *J. Chem. Phys.* **125**, 114302 (2006).
41. Lavert-Ofir, E. et al. Observation of the isotope effect in sub-kelvin reactions. *Nat. Chem.* **6**, 332–335 (2014).

Acknowledgements

This work has been supported by the US Army Research Office under ARO Grant No. W911NF-16-1-1061 and MURI Grant No. W911NF-12-1-0476.

Author contributions

All authors conceived of this study. W.E.P. and N.M. carried out the experimental work. N.M. developed the partial-wave analysis used to interpret the data. All the authors wrote the paper.

Competing interests

The authors declare no competing interests.

Additional information

Supplementary information is available for this paper at https://doi.org/10.1038/s41557-018-0028-5.

Correspondence and requests for materials should be addressed to N.M. or R.N.Z.